

# Adiabatic temperature increase associated with deformation twinning and dislocation plasticity

A. Eisenlohr<sup>\*</sup>, I. Gutierrez-Urrutia<sup>\*</sup>, D. Raabe<sup>\*</sup>

*Max-Planck-Institut für Eisenforschung, Max-Planck-Straße 1, 40237 Düsseldorf, Germany*

Received 9 October 2011; received in revised form 4 March 2012; accepted 4 March 2012

Available online 3 May 2012

## Abstract

We studied local deformation and temperature effects associated with mechanical twinning in Fe–3 wt.% Si at room temperature. During tensile testing, two large stress drops occurred. They were accompanied by local strain and temperature bursts, which we mapped via simultaneous displacement and temperature field characterization. To identify the microstructural origin of these phenomena, we performed high resolution electron backscatter scanning diffraction and electron channeling contrast imaging measurements. The microstructure at the positions where strong adiabatic heating occurred was characterized by the formation of primary twins and high dislocation activity within a range of about 10  $\mu\text{m}$  around the twin–matrix interface. We suggest that the local temperature and strain jumps result from the formation and dissipative motion of lattice dislocations that accommodate twinning.

© 2012 Acta Materialia Inc. Published by Elsevier Ltd. All rights reserved.

**Keywords:** Steel; Twinning; Dislocation; Plasticity; Adiabatic

## 1. Introduction

Irreversible plastic deformation of metals proceeds by dislocation motion and displacive mechanisms such as mechanical twinning or martensitic transformation. The associated deformation energy is predominantly dissipated via defect motion, leading to a distinct thermomechanical response. In metals, this can result in local temperature increases of up to several hundred Kelvin. For example, Chen et al. [1] measured overall temperature increases in Fe–Mn–C steels due to the Portevin–LeChâtelier effect of about 110 °C. Ranc et al. [2] even observed maximum local temperatures of about 1000 °C inside shear bands that formed just before failure during dynamic torsion tests in Ti alloys. Quantifying local dissipative heating is important as it affects thermally activated processes, such as dislocation motion, interface motion, nucleation and strain hardening [3,4], or diffusion-related phenomena, such as

hydrogen embrittlement [5–7]. Many of these thermally activated phenomena depend exponentially on the temperature. This means that deformation-driven local heating can lead to strong kinetic deviations from the material behavior that would be expected from the nominal temperature at which a global test takes place.

The velocities of lattice dislocations and deformation twins can be high, and in some cases can approach the shear wave velocity [8,9]. As the friction stress in metals is rate dependent, high shear rates also lead to a high energy release rate and, hence, higher frictional heating when compared to low deformation velocities.

The instantaneous dissipative heating that occurs during plastic deformation is adiabatic. This means that the heat generation rate is much larger than the heat transfer rate. Hence, the deformation energy released as heat remains in the strained zone for a short time interval, before spreading via heat conductivity. During this time interval, the released heat can be quantified by temperature-sensitive devices.

Thermal imaging has been used to visualize localized plastic effects like shear band motion and the Portevin–Le

<sup>\*</sup> Corresponding authors. Tel.: +49 211 6792 173; fax: +49 211 6792 333.  
E-mail address: [a.eisenlohr@mpie.de](mailto:a.eisenlohr@mpie.de) (A. Eisenlohr).

Châtelier effect in several alloys [1,2,4,10,11], registering instantaneous local temperature increases ranged between 0.5 K and 30 K, and overall temperature increases during testing of 1.5–1000 K. Saai et al. [12] used the temperature response of strained Al bicrystals, together with digital image correlation (DIC) measurements, to compare the observations with a dislocation-based plasticity model. Advanced characterization techniques now allow the instantaneous measurement and evaluation of local temperature and strain changes. Consequently, the thermo-mechanical behavior of material exposed to plastic loads can now be quantified from experiments and incorporated into deformation models. This might lead to a more precise prediction of the mechanical behavior of materials, taking account of adiabatic effects.

Here we report on the deformation-induced heating effects accompanying mechanical twinning in Fe–3 wt.%Si polycrystals. In the present case, deformation twinning occurs abruptly during tensile testing (within less than 0.04 s) and results in a load drop, a local strain jump as recorded by DIC and a local burst in the temperature response. A detailed investigation of the microstructure using electron backscatter scanning diffraction (EBSD) and an advanced scanning electron microscopy technique (electron channeling contrast imaging, ECCI) is employed to link the dissipated heat in the material to the underlying deformation mechanisms. This means that we can map a twinning event directly in terms of its stress, thermal, strain, orientation and dislocation signals. The microstructural evolution is compared to thermal calculations, and the connection between microstructural evolution and the heat released in the material is discussed.

## 2. Experimental methods

The material chosen in this study is the electrical steel Orsi H 0.3 mm, hereafter denoted as Fe–3wt.%Si. The chemical composition in wt.% is listed in Table 1. It is used in final sheet material form after secondary recrystallization. The material has a strong crystallographic Goss texture {110} <001> and a grain size of several millimeters.

Samples of the dimensions shown in Fig. 1 were cut from sheets of  $\approx 0.26$  mm thickness, so that the rolling direction was parallel to the tensile axis. The specimen was tapered to a width of 23.7 mm in order to localize the stress in the center of the specimen.

Tensile tests were performed in a Zwick H100 machine (Zwick AG, Germany) at a constant crosshead speed of  $2 \text{ mm min}^{-1}$ . Temperature changes on the surface of the specimen were measured by means of a thermal camera VarioCAM hr research 680/30 mm (Infratec GmbH,

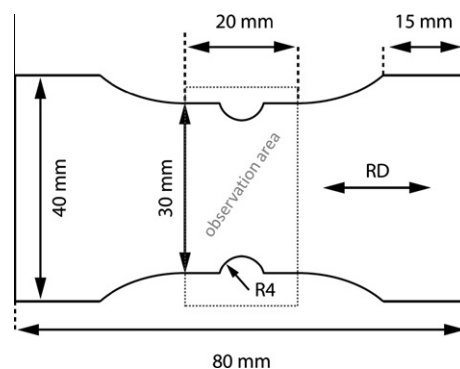


Fig. 1. Tensile specimen shape and dimensions. RD: rolling direction of the original sheet. The taper (R4) was used to promote stress localization in the observation region.

Germany). To minimize the reflected radiation, one specimen surface was coated with black spray paint in order to achieve black body characteristics.

The camera detector is an uncooled microbolometer focal plane array consisting of an arrangement of  $640 \times 480$  elements gathering longwave infrared radiation from  $7.5 \mu\text{m}$  to  $14 \mu\text{m}$ . The device records pictures at a maximum detection rate of 50 Hz. The temperature sensitivity of the thermal camera is specified through the noise equivalent temperature difference equal to 60 mK at 303 K, and its geometric resolution parameter instantaneous field of view is 0.8 mrad. This leads to a maximum spatial resolution of  $160 \mu\text{m}$  per pixel at a distance to the specimen of 0.2 m.

In order to obtain the local strain distribution during the tensile test, two-dimensional DIC was employed [13–16].

The surface pattern required for the DIC was obtained by applying two different color sprays on the sample surface. First, a white spray was used to obtain a homogeneous background, then a black spray was applied to obtain a spotted pattern. The surface was recorded at a rate of 10 Hz by an optical camera (CCD-1300: VDS Vosskühler GmbH, Germany) at a resolution of up to 1300 dpi. The instrument was equipped with a lens of 50 mm focal length and a maximum aperture of 2.8 (Schneider-Kreuznach, 55543 Bad Kreuznach, Germany). The camera set-up was controlled by the ARAMIS software version 6.0.0–3 (GOM – Gesellschaft für Optische Messtechnik mbH, Germany).

Orientation maps were performed in a JSM 6490 tungsten filament scanning electron microscope equipped with a TSL OIM EBSD system. EBSD maps were measured at 15 kV acceleration voltage and a working distance of 25 mm.

ECCI, an advanced scanning electron microscopy technique, was used to image deformation twins and dislocation substructures as in a previous work on austenitic steel [17,18].

A recently reported ECCI set-up [19] was used in this study to obtain ECCI images under controlled diffraction conditions, which enabled an enhanced dislocation and

Table 1  
Chemical composition of the used iron–silicon steel.

Element	Si	Mn	Cu	Sn
Composition/wt. %	3.11	0.082	0.069	0.079

interface contrast. The set-up makes use of the EBSD technique for orienting the crystal into optimal diffraction conditions. ECCI images of dislocations were obtained by orienting the crystal at Bragg condition using a (110)- or (200)-type diffraction vector in a “two-beam” condition. Dislocation densities,  $\rho$ , were determined from ECCI images using the relationship [20]  $\rho = 2N/Lt$ , where  $N$  is the number of dislocation lines intersecting a grid of total line length  $L$  on the corresponding ECCI image and  $t$  is the probe depth. The probe depth under the current conditions (acceleration voltage: 10 kV) is either 50 nm for diffraction vector (110) or 70 nm for diffraction vector (200) [18].

ECCI observations were carried out in a Zeiss Cross-beam instrument (XB 1540, Carl Zeiss SMT AG, Germany) consisting of a Gemini-type field emission gun electron column and a focused ion beam device (Orsay Physics). ECCI was performed at 10 kV acceleration voltage and a working distance of 6 mm, using a solid-state four-quadrant backscattered electron detector. The microscope was run in the “high current” mode and an objective lens aperture of 120  $\mu\text{m}$  was used.

With the simultaneous use of these methods, our aim was to map twinning events synchronously in terms of their stress, thermal, strain, orientation and dislocation signals. This enables us to relate the dissipative heating associated with mechanical twinning to the underlying microstructure evolution. However, it should be emphasized that the various probing and mapping techniques applied to the twinning zones in this study are each characterized by an individual spatial resolution, as outlined above (EBSD, ECCI, IR-based temperature probe, image correlation strain maps). Hence, a one-to-one mapping is not given.

### 3. Results

#### 3.1. Mechanical properties and temperature distribution

Fig. 2 shows the variation of the global stress  $\sigma$  with time for Fe–3wt.% Si at room temperature and at constant crosshead speed of 2 mm min<sup>−1</sup>. Fig. 3 shows the corresponding stress drop data from a set of such experiments conducted on samples with slightly different grain morphology and texture. The stress drops occur in a range between 260 MPa and 320 MPa. The arrow in Fig. 3 indicates the reference data taken from Fig. 2.

The global stress in Fig. 2, which we use in the following as a reference data set, is characterized by two stress drops. The first drop is about 80 MPa and occurs at 320 MPa/11 s. Thereafter, the stress increases steadily until the second stress drop occurs at 500 MPa/22 s. Subsequently, the test was interrupted at 24 s. Stress drops in Fe–Si crystals are associated with twinning; Meyers et al. [21] reported that twinning sets in at stresses beyond 350 MPa in Fe–3wt.%Si polycrystals. This is in fair agreement with the flow stresses of 260 MPa–320 MPa measured at the onset of the first strain/temperature bursts in the current

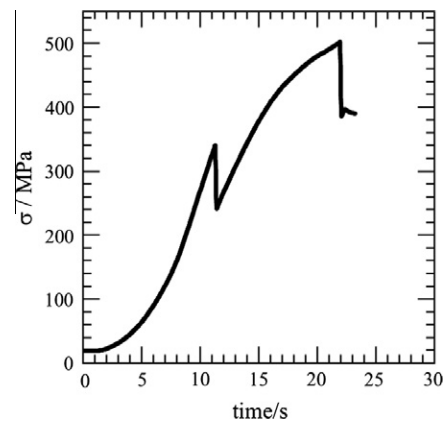


Fig. 2. Evolution of the global stress at the tapered cross-section with time. The test was conducted at constant crosshead speed of 2 mm min<sup>−1</sup> and interrupted after 24 s.

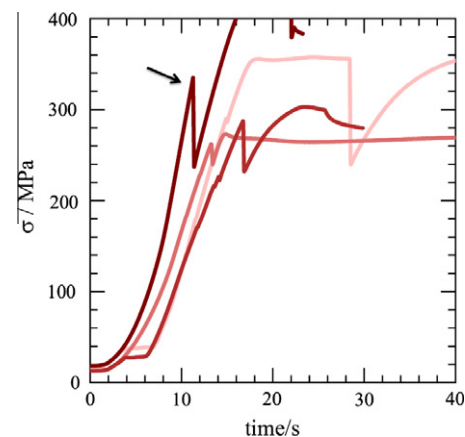


Fig. 3. Stress drop data from a set of experiments conducted on samples with slightly different grain morphology and texture. The stress drops occur in the range between 260 MPa and 320 MPa. The arrow indicates the reference data taken from Fig. 2.

experiments (Fig. 3). The variation in the macroscopic stress value for the onset of twinning is attributed to the dependence on the corresponding orientation and stress concentration factors [17,22].

Fig. 4 shows the variation in the local von Mises strain  $\epsilon$ , determined via DIC (Fig. 4a), and the corresponding local temperature change  $\Delta T = T - T_{\text{ref}}$ , measured via thermal imaging (Fig. 4b), as a function of time for the data shown in Fig. 2. The reference temperature,  $T_{\text{ref}}$ , is defined as the temperature for each pixel taken from the first infrared image at  $t = 0$  s. The two figures show the strain and temperature evolutions during tensile testing at three different sample positions that are marked in Figs. 5 and 6 (cross or circle marks). These maps show the complete temperature and strain patterns on the surface of the sample at the moment of the first and second stress drop, respectively (Fig. 2). The black lines in these figures indicate the grain structure that is overlaid from corresponding EBSD maps. At the marked positions, we investigate the relationship

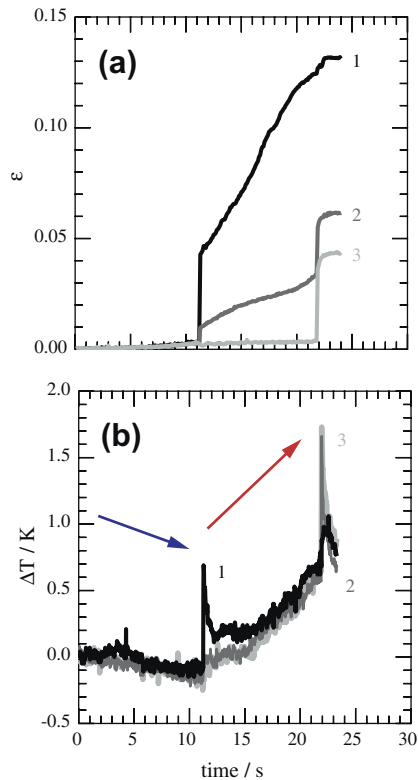


Fig. 4. Temporal evolution of strain and temperature at three different evaluation points during the tensile test shown in Fig. 2. For the positions of the points, see e.g. Fig. 5. (a) Local von Mises strain variation with time measured via digital image correlation. (b) Local evolution of  $\Delta T$  with time obtained from thermal measurements.

between the local plastic events and the associated temperature increments in more detail.

Position 1 is located close to the tapered edge of the specimen inside the region where the first temperature and strain bursts appear. Position 2 is close to the opposite edge of the specimen, at the location where the second heat burst occurs. This point is also affected by the strain localization zone that was associated with the first stress drop. Position 3 is placed in the center of the specimen and relates to the second strain and temperature burst event.

At the beginning of loading, the sample undergoes a homogeneous decrease in temperature of about  $-0.2$  K during an overall strain increment of  $\approx 0.003$  (Fig. 4). This temperature decrease occurs at all three positions. The data in Fig. 4b reveal that the temperature fluctuation in this strain interval is smaller than the overall temperature decay of  $-0.2$  K.

After this modest cooling period, the first global stress drop appears after around 11 s loading time (Fig. 2). It is associated with a sudden and steep increase in both strain and temperature. Point 1 reveals the highest strain increment (0.04), whereas it is smaller at point 2 (0.008) and almost zero at point 3 (see Fig. 4a at 11 s loading time). The average local strain decreases from point 1 to point 2 across the specimen, as illustrated in Fig. 5b. The plastic strain video available online reveals that the plastic strain

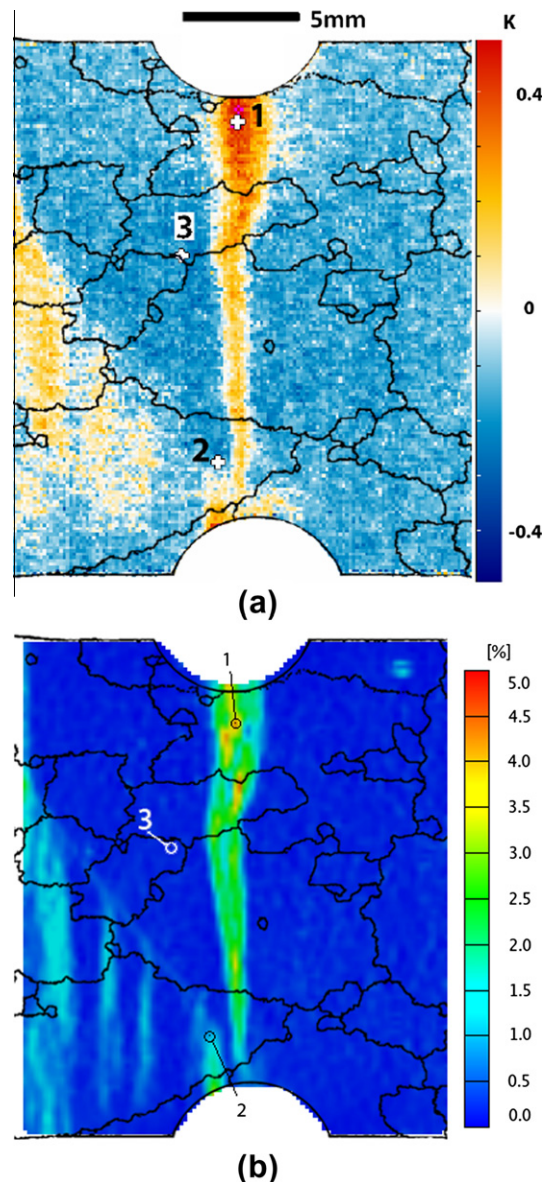


Fig. 5. (a) Local temperature change and (b) local von Mises strain accumulation at about  $t = 11.3$  s. Both images are overlaid with the grain structure that was obtained from an EBSD measurement. Points 1, 2 and 3 correspond to local measurement points for strain and temperature increases in Fig. 4.

burst that is associated with the first stress drop occurs within a very narrow time frame of  $\leq 0.1$  s. The corresponding temperature burst is observed in Figs. 4b and 5a, and also in the video of the temperature evolution available online. Point 1 is associated to the highest temperature increment (0.8 K in 0.04 s). The temperature gradually decreases across the specimen towards position 2. At this point, as well as at point 3, the temperature variation is less significant than at point 1. In particular, these points do not exhibit a sudden burst in temperature. The data also reveal that the twin propagation velocity in the current case is not very high, namely, about  $0.13 \text{ m s}^{-1}$  when considering a time of 0.04 s and a grain size of about 5  $\mu\text{m}$ .



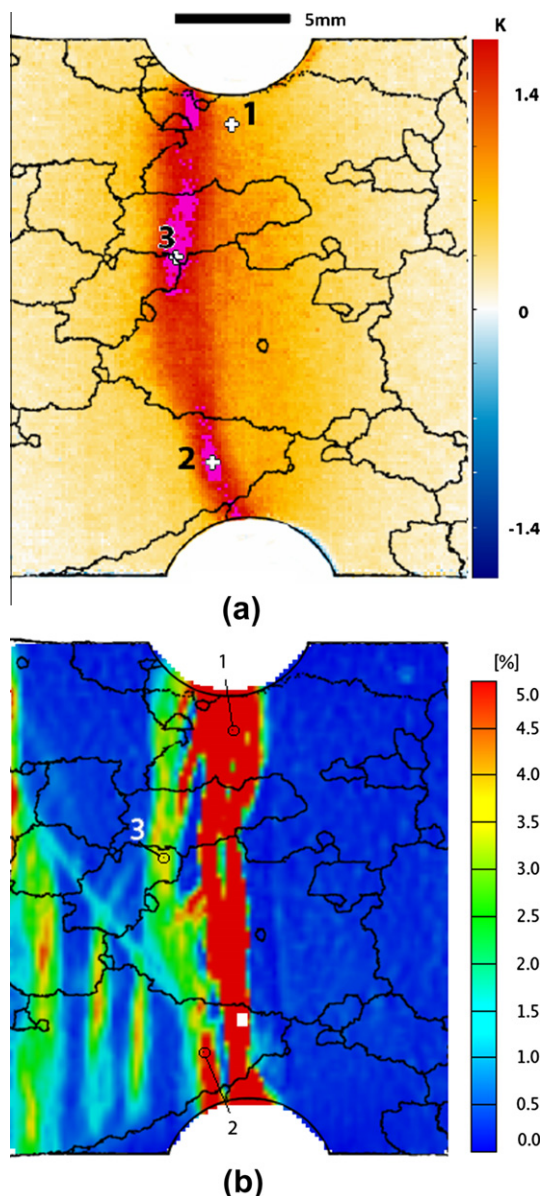


Fig. 6. (a) Local temperature change and (b) local von Mises strain accumulation at about  $t = 21.9$  s. Both images are overlaid with the grain structure obtained from EBSD maps. Points 1, 2 and 3 correspond to local measurement points for the strain and temperature increases of Fig. 4.

It is important to note that this time step also marks a turning point from a weak gradual incipient cooling period ( $<11$  s loading time, blue trend arrow) to a heating period ( $>11$  s loading time, red<sup>1</sup> trend arrow).

Fig. 5 reveals that there is a region outside of the neck that shows strain and temperature bursts at  $t \approx 11$  s as well. However, due to its proximity to the edge of the evaluation region for strain measurements, it will not be considered in the further discussions.

During further loading, before the second stress drop, the strain increases continuously at points 1 and 2 (0.04–0.13 and 0.008–0.03, respectively). The strain increase at position 3 is small, i.e. 0.004. In the time between the two stress drops, the temperature rises continuously across the entire specimen due to the homogeneous plastic deformation of the material (Fig. 4b).

No difference in temperature response in this strain interval between points 1, 2 and 3 is observed due to the slow velocity and uniformity of deformation. Local minor temperature variations are flattened by the high heat dissipation rate.

The second stress drop (Fig. 2) is associated with corresponding increments in both strain and temperature. The magnitude of the second stress drop is larger than that of the first one. At points 2 and 3, the strain and temperature increase during this second burst by about 0.03 K and 1 K, respectively (Fig. 4b). A snapshot of the temperature and strain changes at the instant in time when the second stress drop occurs is presented in Fig. 6. The temperature and strain bursts in Figs. 5 and 6 are clearly not uniformly spread. Furthermore, their direction of propagation changes in accordance with the propagation of twins and associated dislocations due to the orientation differences among the different grains. The temperature and strain evolutions are also shown in the [supplemental videos](#).

While the local strain distribution maps provide valuable information about the deformation patterns and the kinematics, they do not clearly reveal the underlying instantaneous deformation activity that is associated with the deformation burst events accompanying twin formation.

The latter becomes more clear from the  $\Delta T$  distributions in Figs. 5a and 6a. The red zones in the  $\Delta T$  images reveal the places where the highest deformation activity has led to the highest adiabatic temperature increase. While it is unclear from the strain map (Fig. 6b) where the second twinning process started, the  $\Delta T$  map (Fig. 6a) clearly reveals that the hottest spots lie close to points 2 and 3. These positions hence indicate the onset of the twinning burst. With increasing time, the temperature rise  $\Delta T$  abates again due to heat dissipation. Accordingly, only the most recent strong deformation events become visible. Therefore, the differential  $T$  maps provide detailed information about the sequence of twin events in addition to the more integral information provided by the strain maps.

Fig. 7 displays the individual stress–strain curves for the three microstructure positions 1–3 previously described. The stresses and the matching strain values were adapted from the data measured by the tensile machine (global stress values) and the digital image correlation device (microstrains). Dotted lines refer to fast local deformation jumps occurring at about 11 s (red) and 22 s (blue). The 0.2% yield stress is about 200 MPa. Up to a global stress of 320 MPa, the deformation is mainly elastic in nature. After the first twinning event the work hardening rate drops continuously in points 1 and 2, albeit not parallel,

<sup>1</sup> For interpretation of color in Figs. 3–8 and 10–12, the reader is referred to the web version of this article.

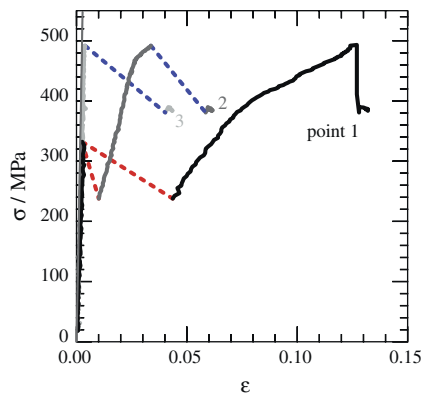


Fig. 7. Stress–strain curve adapted from the overall stress vs. time (Fig. 2) and local strain measurements (Fig. 4a). Dotted lines refer to sudden deformation jumps. Red indicates the first twinning event at around 11 s; blue indicates the second twinning event at around 22 s. (For interpretation of the references to color in this figure legend, the reader is referred to the web version of this article.)

whereas point 3 proceeds to deform at a high work hardening rate.

### 3.2. Dislocation and twin substructure

The deformed substructures and the average dislocation densities at the different positions were observed and analyzed from ECCI images [17,19,22]. Since point 2 is affected by both stress drops (Fig. 7), we focus on points 1 and 3, as their behavior can be attributed to one individual stress drop each.

Point 3 is characterized by a low twinning activity, with a microstructure consisting of primary twins and very few secondary twins (Fig. 8a). We define primary twins as those with the highest Schmid factor for twinning. In this region, the average twin spacing is about 150  $\mu\text{m}$ . Due to the low twinning activity, we assume that the average dislocation density is mainly provided by areas free of twins. Trace analysis conducted on ECCI images combined with high-resolution EBSD maps reveal that the matrix contains a homogeneous dislocation distribution along the  $\{110\}$  and  $\{112\}$  active slip systems. Slip bands with an average spacing of about 2  $\mu\text{m}$  are visible along  $\{112\}$   $\langle 111 \rangle$  slip systems, as illustrated in Fig. 8b. This ECCI image was obtained by tilting the sample, as the matrix is oriented exactly in the Bragg condition for the  $(\bar{1}10)$  diffraction vector. Under this diffraction condition, the matrix appears dark and dislocations appear as sharp bright lines [19]. In particular, slip bands consisting of bright lines (dislocations) are clearly observed. The corresponding simulated diffraction pattern of the surrounding matrix orientation calculated using an algorithm suggested by Zaefferer [23] is shown in Fig. 8c. The average dislocation density estimated from ECCI images ranges between 2 and  $10 \times 10^{13} \text{ m}^{-2}$ .

The microstructure at position 1 is characterized by a higher twinning activity consisting of primary and second-

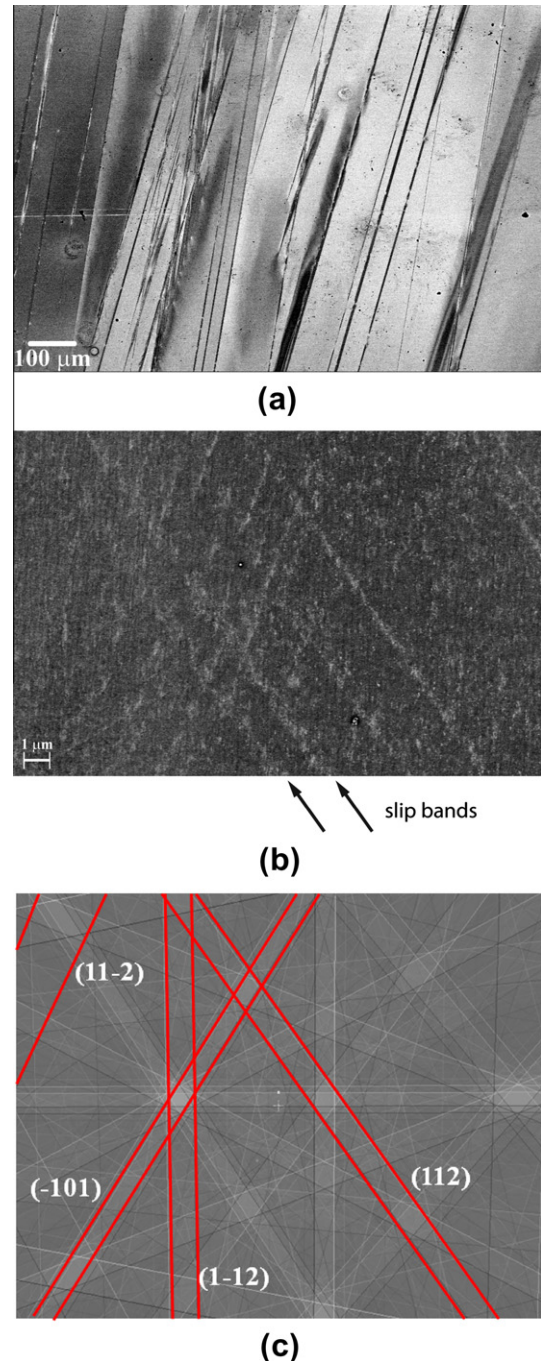


Fig. 8. (a) ECCI image of twin substructure at point 3. (b) ECCI image of dislocation substructure (white sharp lines) at point 3. Slip bands are visible along  $\{112\}$   $\langle 111 \rangle$  slip systems. (c) Calculated diffraction pattern of (b).

ary active twin systems (Fig. 9a). The higher amount of twins is mainly provided by secondary twins nucleated at primary twin interfaces. The average twin spacings of primary and secondary twins are about 150  $\mu\text{m}$  and 25  $\mu\text{m}$ , respectively. Around this position, dislocations are arranged in the form of two zones. The first one, referred to as region 1, is a near-twin region of about 10  $\mu\text{m}$  width and region 2 is the zone beyond this primary matrix layer that interfaces the deformation twins.



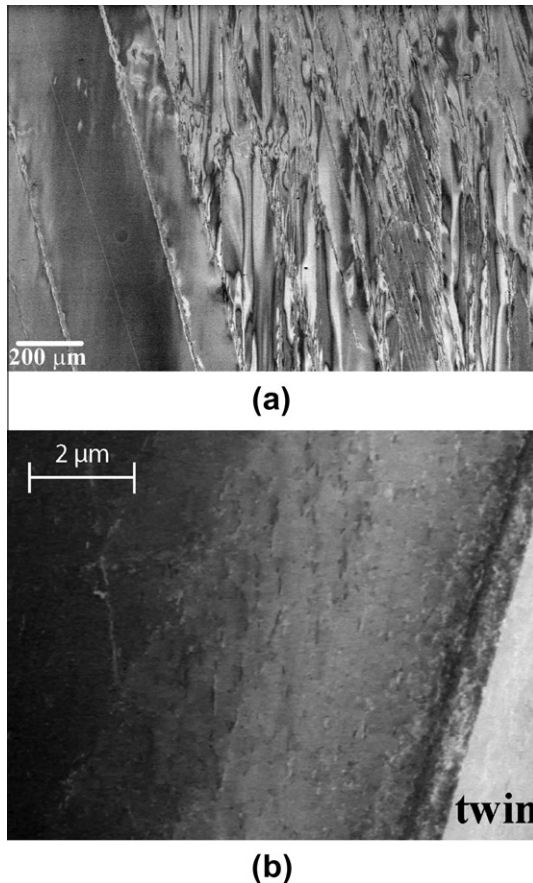


Fig. 9. (a) ECCI image of twin substructure at point 1. (b) ECCI image of dislocation distribution (black and white sharp lines) at the matrix/twin interface corresponding to region 1 of point 1.

Region 1 is characterized by a high average dislocation density, estimated from ECCI images, of about  $10\text{--}20 \times 10^{13} \text{ m}^{-2}$ . The ECCI image of Fig. 9b shows an example of the dislocation distribution around a deformation twin. This image was obtained by tilting the sample so that the crystal matrix that is more remote from the twin interface is oriented exactly in the Bragg position for  $g = 002$ ;  $g$ : diffraction vector. Under this diffraction condition, the matrix appears dark and dislocations appear as bright lines, as shown in the left part of the image. However, due to the number of dislocations created to maintain plastic compatibility at the twin interfaces, lattice rotations around the twin interface are formed. These gradual lattice rotations are accommodated by geometrically necessary dislocations (GNDs) [24–26]. The rotation appears in ECCI images as grayscale gradients. Orientation gradients around twins are clearly visible in the ECCI images (Figs. 8a and 9a) [17,18]. Corresponding high-resolution EBSD maps indicate that these lattice rotations can produce matrix misorientations up to  $10^\circ$  between the bulk matrix and the twin interface. Accordingly, the crystal matrix in the vicinity of the twin interface of Fig. 9b, with about 5 μm extension, is out of Bragg. The bright color of the matrix at the center of the image indicates that the diffraction condition corresponds to  $w < 0$ , where  $w$  is the

deviation vector [27]. Under this diffraction condition, dislocations appear as dark lines. However, dislocations are also visible as bright lines. This can be ascribed to the transition from “two-beam” into “multi-beam” conditions and to electron absorption phenomena [18]. This ECCI image reveals a high density of dislocations of about  $10\text{--}20 \times 10^{13} \text{ m}^{-2}$ , within a zone of 5 μm thickness around the twin interface. It can also be seen that the dislocation density is much higher at the twin interface.

Region 2 is characterized by a homogeneous dislocation distribution with  $\{110\}$  and  $\{112\}$  active slip systems, as illustrated in Fig. 10a. The corresponding slip trace analysis was conducted with the aid of ECCI images combined with high-resolution EBSD. Under the current diffraction condition (close to Bragg for  $g = 110$ ), the matrix appears dark and dislocations appear as sharp bright lines. The corresponding simulated diffraction pattern of the matrix orientation is shown in Fig. 10b. In this region, the average dislocation density estimated from ECCI images ranges between  $2$  and  $6 \times 10^{13} \text{ m}^{-2}$ . A summary of the measured dislocation densities in points 1 and 3 is provided in Table 2.

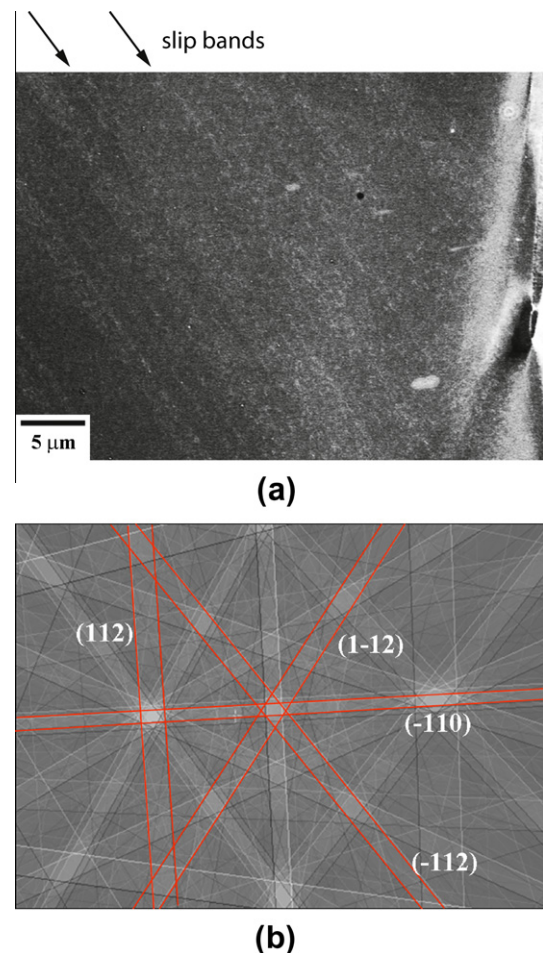


Fig. 10. (a) ECCI image of dislocation distribution (white sharp lines) at region 2 of point 1. (b) Calculated diffraction pattern of (a).

Table 2  
Average dislocation densities determined by ECCI.

Area	Point 1 Region 1	Point 1 Region 2	Point 3
Dislocation density/ $10^{13} \text{ m}^{-2}$	10–20	2–6	2–10

At both evaluation points, the dominant feature is the primary twins. They are commonly wide (about  $5 \mu\text{m}$ ), and span several grains in length. Furthermore, only these primary twins frequently show stress intensities in the form of fracture sites along their longitudinal extension.

#### 4. Discussion

Elastic deformation is associated with an increase in the material's volume.

This effect leads to a temperature decrease  $\Delta T_e$  that, assuming an adiabatic process, can be written as [28]:

$$\Delta T_e = -\frac{\alpha T}{\rho C_p} \Delta \sigma \quad (1)$$

where  $\alpha$  denotes the coefficient of thermal expansion,  $T$  is the initial temperature,  $\rho$  is the material's density,  $C_p$  is the heat capacity at constant pressure and  $\Delta \sigma$  is the change in the sum of the principal stresses. Using the material parameters of Fe–3wt.%Si (Table 3) and a stress increment of 0.32 GPa, Eq. (1) yields a temperature decrease of 0.28 K in the elastic regime. This is slightly larger than the homogeneous average cooling of  $\approx 0.2$  K that was measured in the material just before the onset of plasticity. We attribute this difference to deviations from adiabatic conditions (quasi-static deformation rate causing heat losses through the grips) and the fact that heat dissipation is faster than data acquisition.

With the onset of plastic deformation, the material starts to emit heat instead of absorbing it. The heat generated during dissipative plastic deformation of the material is described by the Clausius–Duhem inequality (also referred to as dissipation inequality):

$$q = \sigma : \dot{\epsilon}^p - A_k \dot{V}_k - \phi \cdot \frac{\text{grad} T}{T} \geq 0 \quad (2)$$

where  $q$  is the dissipative heat that is formed per unit volume and time,  $\sigma : \dot{\epsilon}^p$  represents the plastic work introduced into the material per time,  $A_k \dot{V}_k$  represents the self energy of the lattice defects that are stored inside the material, here

represented as a set  $A_k$  of internal state variables  $V_k$ ,  $\phi$  is the conductive heat flux and  $T$  is the temperature [29]. As will be shown below, defect storage plays a minor role for the energy balance.

Assuming adiabatic conditions, which eliminates the heat flux term  $\phi$ , and introducing  $\beta$  as the fraction of plastic work converted into heat [30], a temperature response  $\Delta T_p$ , associated with the stress drop, can be estimated. The assumption is justified as the dissipative heat generation rate is in the current case much larger than the heat transfer rate.

For this purpose, the plastic work is integrated from  $t_{\text{jump}}$ , where the stress suddenly drops, to  $t_{\text{jump}} + \Delta t$ , where the stress increases again:

$$\Delta T_p = \frac{\beta}{\rho C_p} \int_{t_{\text{jump}}}^{t_{\text{jump}} + \Delta t} \sigma : \dot{\epsilon}^p dt \quad (3)$$

In order to establish upper and lower bounds for the deformation-induced temperature increase in terms of the underlying dislocation mechanisms, two scenarios can be considered.

In the first one (upper bound temperature estimate), we assume that all of the plastic energy is converted into dissipative heat ( $\beta = 1$ ) and none of the work is stored as self energy of crystal defects. Inserting stress and strain values for the two twinning events obtained from the data of Fig. 7, material properties from Table 3 and  $\beta = 1$  into Eq. (3) yields a maximum temperature increase of 3.1 K at point 1 and 4.5 K at point 3. These boundary conditions provide an estimate of the maximum possible dissipative temperature increase.

In the second scenario (upper bound dislocation density), we consider that all of the plastic work introduced in the material is stored as internal energy through the creation of dislocations ( $\beta = 0$ , hence  $\Delta T_p = 0$  K). This estimate results in a dislocation density increase  $\Delta \rho$  of:

$$\Delta \rho = \frac{(1 - \beta)}{0.5Gb^2} \int_{t_{\text{jump}}}^{t_{\text{jump}} + \Delta t} \sigma : \dot{\epsilon}^p dt \quad (4)$$

where  $G$  and  $b$  represent the shear modulus and Burgers vector of the material, respectively. The material properties listed in Table 3 and the plastic work provided by the data of Fig. 7 yield upper bounds for the dislocation density of  $4 \times 10^{15} \text{ m}^{-2}$  and  $6 \times 10^{15} \text{ m}^{-2}$  for points 1 and 3, respectively. We further assume an initial dislocation density of  $\rho = 10 \times 10^{11} \text{ m}^{-2}$  [31].

In order to map these trends more quantitatively, Fig. 11 depicts the local distribution of the dislocation densities estimated for positions 1 and 3, together with the limits calculated from Eqs. (3) and (4). Point 1 shows a measured dislocation density close to the twin–matrix interface of  $10\text{--}20 \times 10^{13} \text{ m}^{-2}$  and  $2\text{--}6 \times 10^{13} \text{ m}^{-2}$  in the matrix away from the twins (Table 2). Due to the high amount of secondary twinning at the primary twin–matrix interface, the area of high average dislocation density is rather wide and gradually decreases to the unaffected

Table 3  
Physical properties of Fe–3wt.%Si.

Property	Symbol	Value	Unit
Coefficient of thermal expansion	$\alpha$	$11.1 \times 10^{-6}$	$\text{K}^{-1}$
Mass density	$\rho$	7650	$\text{kg m}^{-3}$
Heat capacity	$C_p$	480	$\text{J kg}^{-1} \text{K}^{-1}$
Shear modulus	$G$	$8.4 \times 10^{10}$	Pa
Burgers vector	$b$	$2.48 \times 10^{10}$	m
Thermal conductivity	$k$	22	$\text{W m}^{-1} \text{K}^{-1}$



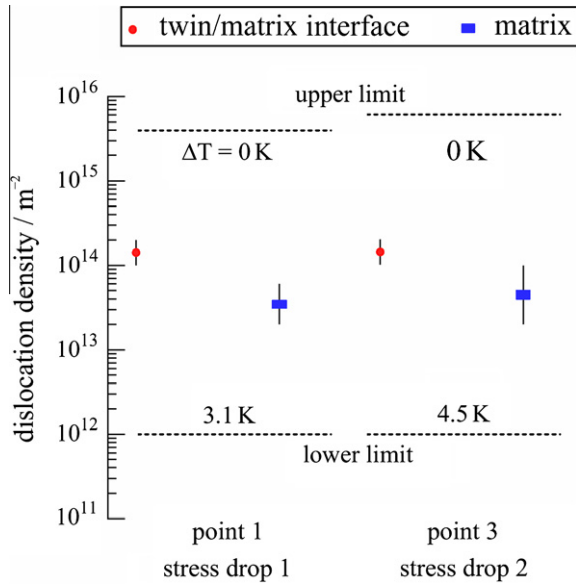


Fig. 11. Measured local dislocation densities at observation points 1 and 3. For each point, we analyzed the dislocation densities close to the twin–matrix interface (red) and more remote (10  $\mu\text{m}$ ) from the interface in the matrix (blue). The upper limit of the dislocation densities (no dissipation; only dislocation storage) and the theoretical maximum temperature changes (complete dissipation; no dislocation storage), each calculated for the respective stress drop at these points, are included as dotted lines. Lower limit: approximated from Ref. [31] (as-annealed state). (For interpretation of the references to color in this figure legend, the reader is referred to the web version of this article.)

matrix value. The estimated dislocation density at point 3 close to the twin–matrix interface is about  $10\text{--}20 \times 10^{13} \text{ m}^{-2}$  and  $2\text{--}10 \times 10^{13} \text{ m}^{-2}$  in the matrix (Table 2). Since only a few secondary twins occur at point 3, the area of high dislocation activity is limited to the region that is affected by the interfaces of the primary twins/matrix (GNDs that accommodate the misorientation and local stress intensity effects). The average dislocation density decrease from the twin–matrix interface into the matrix region is rather steep. The average dislocation density limits calculated according to the energy considerations formulated in Eqs. (3) and (4) are included in Fig. 11 and provide reasonable boundaries for the measured values. The maximum possible increase in the dislocation density (no dissipation; only dislocation storage) is referred to as the upper limit (0 K temperature increase) and the minimum increase (complete dissipation; no dislocation storage) is referred to as the lower limit (3.1 K at point 1 and 4.5 K at point 3) in Fig. 11.

Both the measured temperature increase of 0.7 K or 1.7 K and the dislocation density values at positions 1 and 3, respectively, fall well within the estimated bounds. This means that, in the current case, both contributions play a role in explaining the observed phenomena: namely, the dissipative heating associated with the motion of dislocations (Figs. 4b, 5a and 6a) and the storage of dislocations (Figs. 8–10).

To better understand the microstructural features responsible for the temperature changes in the material,

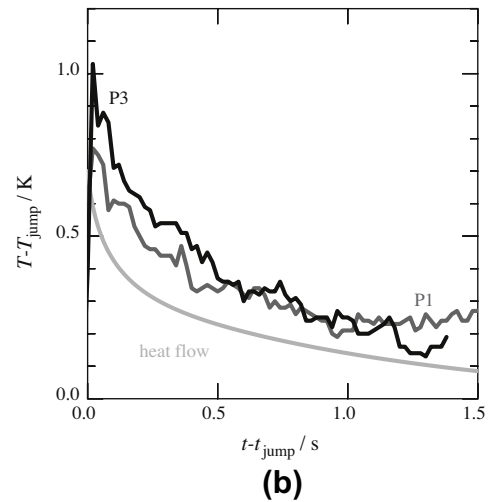
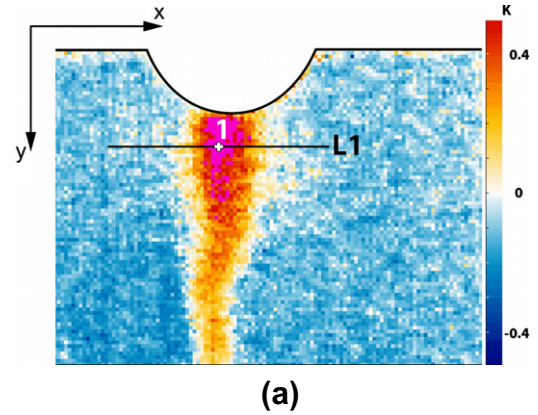


Fig. 12. (a) Coordinate system and location of temperature line profile L1 at point 1 (white cross) for heat flow calculation. (b) Comparison of temperature evolution after jumps 1 ( $\approx 11$  s, point 1) and 2 ( $\approx 22$  s, point 3), and calculated heat flow after jump 1 for point 1.  $T_{\text{jump}}$  and  $t_{\text{jump}}$  are the respective temperature and time values just before the jumps.

the local measured heating at positions 1 and 3 at the respective decay times are compared to each other and to a calculated global heat flow at point 1. The calculation is based on the one-dimensional heat flow equation,

$$\Delta T = \frac{k}{\rho C_p} \frac{\delta T}{\delta x} \Delta t \quad (5)$$

where  $k$  is the thermal conductivity,  $\rho$  is the material's density and  $C_p$  is the heat capacity at constant pressure.  $\frac{\delta T}{\delta x}$  marks the heat flow in the material along the tensile direction  $x$  (direction of the largest temperature gradient) and  $\Delta t$  is the time. As an input for the heat flow, we consider a temperature profile L1, which is extracted from the data of Fig. 5a for point 1 at 11.29 s. The location of this evaluation line, together with the corresponding coordinate system, is illustrated in Fig. 12a. We assume symmetry at point 1 and continuous heat flow at the ends of the profile as boundary conditions. Fig. 12b shows the calculated heat flow at point 1 as a function of the relative time  $t - t_{\text{jump}}$ . We have further included in this figure the experimental temperature evolutions measured at the two stress drops,

denoted as P1 and P3.  $T_{\text{jump}}$  is the temperature value just before the respective temperature jumps.  $t_{\text{jump}}$  corresponds to the time of the sudden temperature rise at points 1 or 3, respectively. At both positions, P1 and P3, the temperature rises by about 0.8–1 K within a time interval of 0.02 s and then abates to a homogeneous temperature distribution in about 1 s. The calculated heat flow, in contrast, shows a very rapid temperature decrease based on the thermal conductivity of the material. It is clear from Fig. 12b that the calculated heat flow abates much faster than the experimental profiles, which are similar to each other in their time-dependent evolution.

This indicates that the temperature response of the material cannot be related to a single temperature jump alone, but to some time-dependent dislocation motion. In the present material, the only dislocation sources showing a time-dependent behavior are those associated to the twin interfaces.

However, as Figs. 8, 9 and 11 show, although points 1 and 3 contain different dislocation and twin substructures and, accordingly, different dislocation density distributions, the temperature variation at these points is rather similar.

The high average dislocation density observed in the vicinity of the twin interfaces, about  $10\text{--}20 \times 10^{13} \text{ m}^{-2}$ , is attributed to the requirement for plastic compatibility (accommodation deformation) and to dislocation–twin interface interactions [22,24,32,33]. The motion of twin interfaces through the crystal matrix requires the generation of dislocations to maintain plastic compatibility at the twin interface [8]. Furthermore, crystal lattice rotations around twin interfaces are formed to maintain plastic compatibility between the twinned material and the surrounding matrix. These lattice rotations are accommodated by GNDs. Rotations of a few degrees in the vicinity of the twins have been measured by EBSD and are visible as orientation gradients in the ECCI images. However, when

considering that the movement of twin interfaces occurs through the already deformed crystal, dislocation–twin interface interactions must be considered.

Priestner and Leslie [32] have shown that, under local stress concentrations, twin or cleavage nucleation can occur at the intersection of  $\{112\}$ -type slip bands in body-centered cubic metals. The piling-up of glide dislocations along  $\{112\}$  slip planes against a  $\langle 001 \rangle$ -type dislocation barrier leads to high stress concentrations and dislocation dissociation. Depending on the resulting stress state, the dissociation product can lead to a three-layer twin or a barrier configuration similar to that of a Lomer–Cottrell lock in face-centered cubic metals. In the latter case, this barrier configuration is sufficiently strong to allow cleavage nucleation. Accordingly, these processes, namely deformation twinning and cleavage fracture, are competitive mechanisms that can be nucleated at the same site. As Figs. 8b and Fig. 10a reveal, the crystal matrix contains a large amount of  $\{112\}$ -type slip bands. The interaction of these slip bands with twin dislocations, which glide along  $\{112\}$  planes, may therefore promote twinning (secondary twinning) or cleavage fracture at intersection sites.

ECCI observations at both evaluation points 1 and 3 reveal that primary twin interfaces are frequently affected by the interaction with  $\{112\}$ -type slip bands, as Fig. 13 indicates. These interaction zones can even lead to local cleavage nucleation.

Associated with these intersection regions, the ECCI images reveal, when used at optimum diffraction conditions, a high density of dislocations distributed along the slip bands, with a maximum at the fractured twin interfaces (see inset in Fig. 13). This analysis shows that the magnitude of the shear stresses that occur at the tip of the intersection edges or at nucleated cracks act as highly active dislocation sources. We therefore ascribe the similar temperature variations measured at both points 1 and 3 by thermal imaging, to dislocation sources that are formed at the primary twin interfaces due to twin–slip band intersections. This interface source-related sudden movement of many dislocations at the fracture sites of the twin interfaces is assumed to be the main source of the temperature jumps that we observed during the twinning events.

## 5. Conclusions

We have studied the mechanical behavior at room temperature of a Fe–3wt.%Si polycrystal. We analyzed the local mechanical response by DIC and the microstructure by EBSD and ECCI at two specific positions corresponding to two distinct stress drops in time. The following conclusions are drawn:

- The global stress–strain behavior exhibits two stress drops, of about 80 MPa in the first case and 110 MPa in the second case. These stress drops are accompanied by local temperature and strain bursts related to twin formation.



Fig. 13. ECCI analysis that reveals edges in the primary twin–matrix interface. These are associated with stress intensities that create large orientation gradients (ECCI brightness gradient). Inset: ECCI close-up of probable cleavage fracture nucleation site at primary twin–matrix interface.

- Evaluation point 1, corresponding to the first stress drop, is characterized by a high twinning activity of large primary and smaller secondary twins. The interfaces of the primary twins and the matrix show a high dislocation density,  $10\text{--}20 \times 10^{13} \text{ m}^{-2}$ , and frequent appearance of stress intensities at these interfaces.
- Evaluation point 3, corresponding to the second stress drop, is characterized by the presence of primary twins only accompanied by high dislocation activity and stress intensities at the interfaces. Due to the lower twinning activity at point 3, the matrix shows a higher overall dislocation activity.

The evaluation of the local strain evolution shows an instantaneous strain increment accompanying the global stress drop related to the twin formation and a simultaneous burst in temperature. The temperature suddenly rises by about 1 K within 0.04 s, in addition to the global dissipative heating of the specimen due to the homogeneous plastic deformation at each evaluation point.

The results of the thermal calculations suggest that this temperature jump is correlated with the highly localized formation and movement of dislocations, leading to an increase in dislocation density close to the twin–matrix interface. The ECCI measurements performed at the primary twin–matrix interface show the frequent appearance of strain localization and fracture sites accompanied by a sharp increase in dislocation density. Therefore, we suggest that the measured jump in temperature is mainly due to the dislocation structure evolving in or close to the interfaces between the large primary twins and the abutting matrix.

### Acknowledgement

The authors gratefully acknowledge financial support from the Deutsche Forschungsgemeinschaft under project DFG EI681/3-1.

### Appendix A. Supplementary data

Supplementary data associated with this article can be found, in the online version, at <http://dx.doi.org/10.1016/j.actamat.2012.03.008>.

### References

- [1] Chen L, Kim H-S, Kim S-K, De Cooman BC. *ISIJ Int* 2007;47:1804–12.
- [2] Ranc N, Taravella L, Pina V, Herve P. *Mech Mater* 2008;40:255–70.
- [3] Estrin Y, Kubin LP. *Mater Sci Eng* 1983;57:137–42.
- [4] Allain S, Cugy P, Scott C, Chateau J-P, Rusinek A, Deschamps A. *Int J Mater Res* 2008;99(7):734–8. <http://dx.doi.org/10.3139/146.101693>.
- [5] Lecoester F, Chene J, Noel D. *Mater Sci Eng A* 1999;262:173–83.
- [6] Kim YS. *Mater Sci Eng A* 2007;468–470:281–7.
- [7] Song J, Curtin WA. *Acta Mater* 2011;59:1557–69.
- [8] Meyers MA. *Mater Sci Eng* 1981;51:261–3.
- [9] Cottrell AH, Bilby BA. *Philos Mag Ser* 1951;7(42):573–81.
- [10] Guduru PR, Rosakis AJ, Ravichandran G. *Mech Mater* 2001;33:371–402.
- [11] Louche H, Vacher P, Arrieux R. *Mater Sci Eng A* 2005;404:188–96.
- [12] Saai A, Louche H, Tabourot L, Chang HJ. *Mech Mater* 2010;42:275–92. <http://dx.doi.org/10.1016/j.mechmat.2009.11.011>.
- [13] Ma A, Roters F, Raabe D. *Acta Mater* 2006;54:2181–94.
- [14] Raabe D, Sachtleber M, Zhao Z, Roters F, Zaefferer S. *Acta Mater* 2001;49(17):3433–41. [http://dx.doi.org/10.1016/S1359-6454\(01\)00242-7](http://dx.doi.org/10.1016/S1359-6454(01)00242-7).
- [15] Sachtleber M, Zhao Z, Raabe D. *Mater Sci Eng A* 2001;336:81–7.
- [16] Roters F, Eisenlohr P, Hantcherli L, Tjahjanto DD, Bieler TR, Raabe D. *Acta Mater* 2010;58:1152–211. <http://dx.doi.org/10.1016/j.actamat.2009.10.058>.
- [17] Gutierrez-Urrutia I, Zaefferer S, Raabe D. *Mater Sci Eng A* 2010;527:3552–60.
- [18] Gutierrez-Urrutia I, Raabe D. *Scripta Mater* 2012;66:343–6.
- [19] Gutierrez-Urrutia I, Zaefferer S, Raabe D. *Scripta Mater* 2009;61:737–40.
- [20] Ham RK. *Philos Mag* 1961;69:1183–4.
- [21] Meyers MA, Vöhringer O, Lubarda VA. *Acta Mater* 2001;49(19):4025–39.
- [22] Gutierrez-Urrutia I, Raabe D. *Acta Mater* 2011;59:6449–62.
- [23] Zaefferer S. *J Appl Crystallogr* 2000;33:10–25.
- [24] Demir E, Raabe D, Zaafarani N, Zaefferer S. *Acta Mater* 2009;57:559–69.
- [25] Zaafarani N, Raabe D, Singh RN, Roters F, Zaefferer S. *Acta Mater* 2006;54:1863–76.
- [26] Ma A, Roters F, Raabe D. *Acta Mater* 2006;54:2169–79.
- [27] Spencer JP, Humphreys CJ, Hirsch PB. *Philos Mag* 1972;26:193–213.
- [28] Pandey KN, Chand S. *Int J Press Ves Pip* 2003;80:673–8.
- [29] Bouferra R, Pron H, Henry J-F, Bissieux C, Beaudoin JL. *Int J Thermal Sci* 2005;44:115–9.
- [30] Zhang B, Shim VPW. *Int J Impact Eng* 2010;37:50–68.
- [31] Griffiths D, Riley JN. *Acta Metall* 1966;14:755–73.
- [32] Priestner R, Leslie WC. *Philos Mag* 1964;11(113):895–916. <http://dx.doi.org/10.1080/14786436508223953>.
- [33] Nabarro FRN. *The international series of monographs on physics*. Oxford University Press; 1967.